Heliyon 5 (2019) e02522

Contents lists available at ScienceDirect

Heliyon

journal homepage: www.heliyon.com

The effect of alloying elements on the properties of pressed and non-pressed biodegradable Fe–Mn–Ag powder metallurgy alloys

Malcolm Caligari Conti [a,*], Bertram Mallia [a], Emmanuel Sinagra [b], Pierre Schembri Wismayer [c], Joseph Buhagiar [a], Daniel Vella [a]

[a] Department of Metallurgy and Materials Engineering, Faculty of Engineering, University of Malta, Msida, MSD 2080, Malta
[b] Department of Chemistry, Faculty of Science, University of Malta, Msida, MSD 2080, Malta
[c] Department of Anatomy, Faculty of Medicine and Surgery, University of Malta, Msida, MSD 2080, Malta

ARTICLE INFO

Keywords:
Materials science
Surgery
Materials application
Materials characterization
Materials synthesis
Biophysical chemistry
Musculoskeletal system
Orthopedics
Rehabilitation
Biodegradable
Corrosion
Non-pressed
Sintering
Fe–Mn–Ag
Pressed
Powder metallurgy
Fe Mn
Scaffolds

ABSTRACT

Current trends in the biodegradable scaffold industry call for powder metallurgy methods in which compression cannot be applied due to the nature of the scaffold template itself and the need to retain the shape of an underlying template throughout the fabrication process. Iron alloys have been shown to be good candidates for biomedical applications where load support is required. Fe–Mn alloys were researched extensively for this purpose. Current research shows that all metallurgical characterisation and corrosion test on Fe–Mn and Fe–Mn–Ag non pre-alloyed powder alloys are performed on alloys which are initially pressed into greens and subsequently sintered. In order to combine the cutting-edge field of biodegradable metallic alloys with scaffold production, metallurgical characterisation of pressed and non-pressed Fe, Fe–Mn and Fe–Mn–Ag sintered elemental powder compacts was carried out in this study. This was performed along with determination of the corrosion rate of the same alloys in *in vitro* mimicking solutions. These solutions were synthesised to mimic the osteo environment in which the final scaffolds are to be used.

Both pressed and non-pressed alloys formed an austenite phase under the right sintering conditions. The corrosion rate of the non-pressed alloy was greater than that of its pressed counterpart. In a potentiodynamic testing scenario, addition of silver to the alloy formed a separate silver phase which galvanically increased the corrosion rate of the pressed alloy. This result wasn't replicated in the non-pressed alloys in which the corrosion rate was seen to remain similar to the non-silver-bearing alloy counterparts.

1. Introduction

A number of parameters need to be taken into consideration when designing a biodegradable bone scaffold including (1) biocompatibility, providing for cell attachment and growth, (2) biodegradability, such that the scaffolds can be safely substituted by osteoid deposition, (3) good mechanical properties, to withstand loading in the area of application, be it tensile compressive or bending, (4) the ability of the scaffolds to provide innate antibiotic response and/or sterilibility without the loss of all other mentioned functions and (5) being non-ferromagnetic [1, 2]. Iron alloys have been shown to be good candidates for bio-medical degradable scaffolding applications where load support is required. Fe–Mn alloys have been researched extensively for this purpose [2]. The transformation of a ferritic to austenitic iron based alloy is accomplished by manganese addition to iron. An addition of up to 20 wt.% Mn gives a bi-phasic structure, consisting of both austenite and martensite phases [3]. Increasing the percentage manganese content to and above 25 wt.% transforms the microstructure to a single-phase austenitic microstructure [3]. This transformation ensures that the alloy is completely non-ferromagnetic and thus magnetic resonance imaging (MRI) compatible [4].

A manganese content greater than 15 wt.% has been shown to transform the final post-sintered microstructure to a partially austenitic microstructure when the green is pressed before sintering [4, 5], but to the best of the authors' knowledge no metallurgical characterisation has been conducted on non-pressed non-pre-alloyed powder metallurgy parts. However, pressing may not always be possible when forming a metallic alloy bone scaffold. In effect, when considering three

* Corresponding author.
E-mail address: mcali01@um.edu.mt (M. Caligari Conti).

https://doi.org/10.1016/j.heliyon.2019.e02522
Received 26 March 2019; Received in revised form 30 June 2019; Accepted 23 September 2019

dimensional scaffold generation, a widely used technique utilises a polymer "sponge" like structure with interconnected pores [6]. This sponge is dipped in a solution composed of a lubricant, a binder and metallic particles until it is coated. The coated sponge then goes through a heating cycle in order to burn off the polymer sponge and sinter the metallic deposits, thus forming a porous structure in the same shape as the sponge [7, 8, 9]. Given the nature of the sponge and the process, no pressing of the metallic particles takes place after the sponge has been coated. Many of the studies related to the generation of metallic scaffolds through the coating of polymer sponge-like structures, have been limited to powders which were either elemental or pre-alloyed [7, 8, 9]. Thus, a question arises as to whether single element particles would be able to produce the austenitic phase alloy required by the *in vivo* application without the need for pressing. In this study, although elemental powders are still used, a mixture of elements is utilised with the aim of generating an alloy. This presents a novel area of study which would allow the development of 3D Fe-alloy scaffolds from elemental powder mixtures and 3D template scaffolds. If successful, this novel approach may improve resorbable scaffold fabrication by simplifying the process of manufacturing 3D scaffolds from pre-fabricated polymer templates. This is because powders would not have to be pre-alloyed prior to the sintering process.

In relation to the above area of application, the first hypothesis states that the addition of concentrations equal to or higher than 30% Mn to Fe utilised in a non-pressed non-pre-alloyed sintered powder metallurgy component, permits the production of a fully austenitic microstructure.

Several authors have focused on increasing the corrosion rate of pure iron by alloying [3, 7, 10] and the creation of microgalvanic couples through the use of noble elements [11, 12]. Addition of Mn to Fe has the effect of reducing the overall corrosion resistance of the alloy when exposed to *in vitro* solutions which simulate the *in vivo* scenario [3, 7, 10]. Mn addition thus helps to bring the corrosion rate closer to the time required to rebuild the bone structure, providing for reduced stress shielding problems. To this end, Hermawan et al. [13] show that pure iron had a corrosion rate of 14 $\mu A/cm^2$ in modified Hank's solution and this rose to 105.6 $\mu A/cm^2$ in the same electrolyte when 35% Mn was added to the sample composition. The addition of cathodic elements such as palladium and silver increases the corrosion rate of pressed and sintered iron based alloys, and this increase is attributed mainly to the galvanic effect of the cathodic element inclusions on the Fe–Mn grains [11, 12]. However, it is observed that with palladium, the increase in corrosion was not accompanied by an increase in the mass of material lost from the alloy. Rather, the weight was found to remain constant due to the corrosion products adhering to the surface, which in turn causes large variations in the corrosion performance of the alloy [11]. With silver, the galvanic effect is not as pronounced, since the potential of silver is closer to Fe and Fe–Mn alloy compared to other cathodic elements such as palladium [14, 15, 16]. Research in this regard is currently focused exclusively on the corrosion rate of pressed and sintered Fe, Fe–Mn and Fe–Mn–Ag powder coupons. Thus, another aim of this work is to identify differences in corrosion rate between the latter coupons and the novel non-pressed sintered alloy coupons.

The second hypothesis for this work, postulates that the addition of silver to the same non-pressed non-pre-alloyed Fe–Mn alloy would increase the alloy's corrosion rate. This would enable the rate of corrosion of the Fe–Mn alloys to become closer to the rate of osteogenic repair *in vivo*.

Silver is widely used in several products throughout the medical industry including sanitary products [17] and silver bearings [12]. Several authors have shown that minor concentrations of silver (<2 mg/L) in the human host do not cause any cytotoxic effect [17]. On the other hand increasing the concentration of silver ions *in vivo* causes severe toxicity and unfavourable host response [17].

2. Methodology

Iron powder with a purity of 99% (US Research Nanomaterials Inc, USA) was mixed with manganese powder (VWR, International) and high purity silver powder (VWR, International) with specifications as given in Table 1. The ratios in which the powders were mixed are presented in Table 2 in order to produce Fe, Fe–30Mn, Fe–35Mn, Fe–29Mn–2Ag and Fe–28Mn–5Ag coupons. The ratio of Fe:Mn of the silver bearing powders was set at 0.3 since this ratio produced austenite reflections when preliminary X-ray diffractograms were analysed from the non-silver-bearing samples with the same Fe:Mn ratio (Fe–30Mn). The diffractograms for the Fe–35Mn and Fe–30Mn alloy were similar, and thus a lower Mn ratio was selected for the production of the silver bearing alloys. The Fe:Mn ratio was therefore kept constant even when adding silver, in order that the Fe based phase composition does not vary.

The schematic diagram of the sample preparation procedure is shown in Fig. 1. In this study, 24 mixtures of each sample listed in Table 2 were weighed and stored in separate 15 mL volume centrifuge tubes. The tubes were filled to approximately one third of their total volume. Homogeneous powders were obtained after 12 h of mixing in a 3D tumbler (Inversina, Switzerland). Two zirconia balls were then added to each tube in order to act as tumblers such that the powder is mixed more thoroughly. The balls were then removed manually and samples were then sub-divided into 2 sets of 14 tubes each. The first set was stored in a dessicator, while the second set was moved to further processing by compression using a 25 Tonne compression testing rig (Instron, USA). The contents of each tube were placed in a 20 mm diameter die (REFLEX Analytical, USA) and compressed to a pressure of 1.22 GPa at the rate of 0.02 GPa/s to produce greens of approximately 7 mm thickness. This procedure was repeated for all the samples. The sample orientation in the press was also noted as "Top" and "Bottom" with the "Top" surface being the surface closest to the die plunger.

The non-pressed samples were transferred to 20 mm internal diameter, cylindrical, hollow, stainless steel moulds coated with titanium nitride both on the inner and outer surface. This coating acted as a barrier between the stainless steel tubes and the mixture of powders within them. This prevented any welding between the powders and the tube such that no diffusion of elements could take place to or from the powder sample and the tube. The coating also facilitated easy removal of the sample from its holder.

2.1. Sintering process

The powder filled tubes were placed atop an alumina plate. The pressed greens were then rested on the same alumina plate with the bottom of the sample facing the alumina plate and the whole plate transferred to a tube furnace (Nabertherm, Germany). The heating cycle was set to raise the temperature to 1200 °C with a ramp rate of 0.05 °C/s, hold the temperature for 2 h and then cool to room temperature over 12 h with the tube end closed. The shielding gas is composed of 95% nitrogen and 5% hydrogen. The flow rate was set to 100 L/h. The sintered pressed samples produced had a diameter of 20 mm and a height of 7 mm, whilst the unpressed sintered samples had a diameter of 19 mm with an approximate height of 12 mm. The height of the latter samples varied due to the surface irregularity.

After the sintering process, each of the pressed and sintered samples were ground to a finish of P2500 using silicon carbide grinding paper (Metprep, UK) and polished to a finish of 3 μm polycrystalline diamond

Table 1
Powder product code, size and purity.

Powder	Fe Powder (g)	Mn Powder (g)	Ag Powder (g)
Powder product code	Fe 99% 45 μm	VWR 45098-A1	VWR 11402-30
Powder size	45 μm	<10 μm	4–7 μm
Purity	99%	99.6%	99.9%

Table 2
Elemental powder ratios used for Fe, Fe–30Mn, Fe–35Mn, Fe–29Mn–2Ag and Fe–28Mn–5Ag coupons.

Sample nominal composition and name	Fe Powder (g/wt.%)	Mn Powder (g/wt.%)	Ag Powder (g/wt.%)	Mn:Fe Ratio
Fe	18.0/100.0	0.0/0.0	0.0/0.0	0.00
Fe–30Mn	12.6/70.0	5.4/30.0	0.0/0.0	0.30
Fe–35Mn	11.7/65.0	6.3/35.0	0.0/0.0	0.35
Fe–29Mn–2Ag	12.3/68.3	5.3/29.4	0.4/2.2	0.30
Fe–28Mn–5Ag	12.0/66.7	5.1/28.3	0.9/5.0	0.30

(Struers, International) on both the top and bottom faces. The unpressed samples were finished to the same specification solely on the bottom surface due to a highly irregular top surface owing to a lack of green formation prior to the sintering process.

2.2. Microstuctural analysis

The phases present in both the non-pressed and pressed samples were analysed using a X-ray diffractometer (Bruker, USA), having a Cu-Kα source and set up to take readings in the Bragg-Brentano geometry. The diffractogram was obtained by sweeping through 2θ angles ranging between 20° and 120° at 0.6°/min for both as polished surfaces of the pressed coupons and for the bottom as polished surface of the unpressed coupons. The penetration depth of the X-Rays in this particular geometry is expected to be in the range of 15 μm–25 μm [18], however this range may be attenuated due to iron fluorescence radiation when using a Cu-Kα source. Only the bottom surfaces of the unpressed coupons were scanned due to the irregularity of the top surface. Extensive grinding or cutting of the top surface would inevitably remove all evidence of the phases in the top surface and also induce stresses into the sample's microstructure which would have inevitably altered the diffractogram of the newly exposed surface.

The samples were also analysed in a Field-Emission Scanning Electron Microscope (Zeiss, International). A secondary electron detector was used to obtain data on topography and to determine the surface morphology. An electron backscatter detector was used to give data regarding the composition of the alloy in terms of elemental and phase contrast. The images were then processed using ImageJ software in order to estimate the percentage porosity of the sample by area. Energy dispersive X-ray spectrometry (EDS) was also used to obtain a semi-quantitative representation of the concentration of elements present in the powder metallurgy part.

2.3. Corrosion testing

Bone is composed of 20% [19] to 30% [20] protein. Out of this protein content 90% is collagenous protein [21] with the remaining 10% thus being non-collagenous protein. Thus, if an average bone protein content of 25% had to be taken, 2.5% of bone is composed of non-collagenous protein. A buffered salt solution similar to *in vivo* with a protein concentration (25 g/L) would be used as the electrolyte of choice for corrosion testing throughout the study for the *in vitro* simulation of the skeletal environment. This electrolyte was synthesised by adding 25 g bovine serum albumin (BSA) (Sigma Aldrich, International) to 1 L of phosphate buffered saline (PBS) solution (Applichem, Germany). This electrolyte is referred to as "PBS + BSA" throughout this work. A second electrolyte composed solely of PBS solution without BSA was used for comparative purposes in the static immersion tests and henceforth will be referred to as "PBS". Two kinds of corrosion tests were performed; potentiodynamic tests (PDT) and static immersion degradation tests (SIDT).

2.4. Potentiodynamic testing

Potentiodynamic testing was performed on both faces of the pressed and sintered samples finished to a 0.02 μm polish using a Gamry Ref 600 Potentiostat (Gamry, USA) with a three-electrode set up. The un-pressed samples had extensive connected porosity which allowed the solution to infiltrate their thickness rendering electrochemical corrosion testing and evaluation problematic due to leaks of the electrolyte solution onto the brass tightening screw of the setup. The reference electrode consisted of a standard calomel electrode (SCE) inside a luggin capillary probe, while a platinum electrode was used as a counter electrode with the test samples acting as the working electrode.

A working area of 0.63 cm^2 was exposed to 300 mL of solution and a

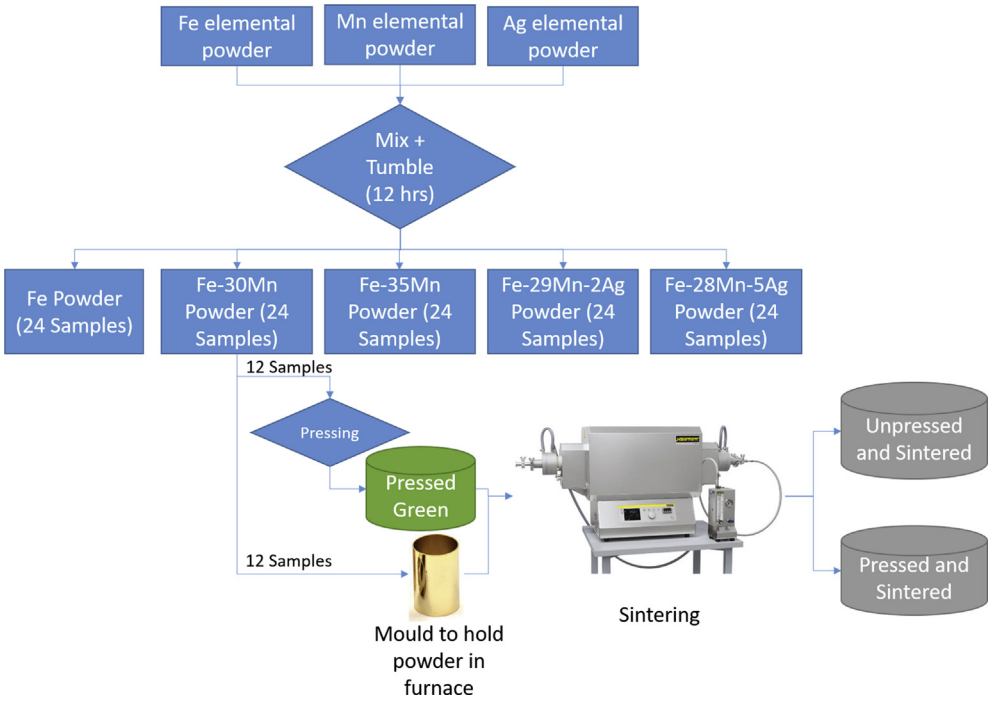

Fig. 1. Schematic diagram of the sample preparation procedure.

solution temperature of 37 ± 1 °C was maintained for the duration of the potentiodynamic test. The open circuit potential (OCP) was left to stabilise for 1 h and was followed by a potentiodynamic sweep from -0.2 V versus OCP to 0.2 V versus OCP at a scan rate of 0.167 mVs^{-1}. This potential range was selected in order that the testing and analysis could be carried out in accordance with ASTM G59 [22] for the determination of corrosion current. Several repeats spread out over 7 days were performed for each sample condition until 3 superimposed plots were obtained. This was done in order to be able to extract numerical conclusions from this testing regime.

The corrosion current (I_{corr}) was calculated from the anodic and cathodic Tafel slopes and the polarisation resistance according to ASTM G102-89: *Standard Practice for Calculation of Corrosion Rates and Related Information from Electrochemical Measurements*.

2.5. Static immersion

Static immersion degradation testing was performed in order to analyse the corrosion in sterile filtered protein bearing (PBS + BSA) and non-protein bearing (PBS) solutions over a period of 14 days. The time period and method was selected so that the results could be compared to those already present in literature [23]. The solutions were sterilised using a 0.22 μm filter (Sterivex, Merck Millipore, USA). 30 aliquots of 100 mL of each of the solutions were then placed in sterilised 100 mL media bottles.

The non-pressed and pressed samples with diameters of 19 mm 20 mm, respectively heights of 12 mm and 7 mm respectively were ground to a finish of P1200 silicon carbide grinding paper (Metprep, UK) and stored under vacuum until the start of the test. 60 samples were prepared in total with 3 samples for each alloy tested in the non-pressed and pressed states. Just before the test, the samples were weighed using a weighing balance (404A, Precisa, Switzerland). The sample was dipped in ethanol (70%) for 1 min and then placed in the media bottle filled with the solutions. This was done in order to sterilise the coupon prior to dipping in sterile media. The bottles were then capped with a modified cap assembly which included a 0.45 μm syringe filter (Sigma Aldrich, International) in order to allow gaseous exchange within the CO_2 incubator. The 18 bottles were then stored in an incubator (Leec, UK) for 14 days which was maintained at 6 vol.% CO_2 and 37 °C. All sample handling was carried out in a laminar air flow hood (Faster, Italy) in order to maintain sterility.

After the 14-day period had elapsed, each of the samples were brought out of the media and gently dipped into deionised water for 15 min to dissolve and remove the salts and proteins. The samples were then dried in a vacuumed tube furnace at 50 °C for 12 h and subsequently weighed. The samples were seen to gain weight as suggested by several authors in literature [11, 12]. The weight of the adhering corrosion product was thus calculated using Eq. (1).

$$Corrosion\ \ Product\ \ Weight = Weight\ \ After - Weight\ \ Before \tag{1}$$

The weight of metal lost to the corrosion product was then calculated using Eq. (2). It was assumed that the salt and protein content of the sample was completely removed by the rinsing cycle.

$$Metal\ \ lost = \frac{Corrosion\ \ Product\ \ Weight}{Oxide\ \ molar\ \ mass} \cdot Alloy\ \ molar\ \ mass \tag{2}$$

The Fe_2O_3 and MnO were assumed to be formed in a ratio identical to the Fe and Mn ratio in each alloy. Silver was assumed not to form an oxide. The values used are tabulated in Table 3.

3. Results

3.1. X-ray diffraction

X-ray diffractograms of pre-sintered Fe coupons (Fig. 2) show a ferrite phase. The diffractograms for Fe–30Mn and Fe–35Mn coupons show a mixture of ferrite and β-Manganese phases.

X-ray diffractograms of the sintered Fe, Fe–30Mn and Fe–35Mn alloys are presented in Fig. 3. This figure shows that the Fe–30Mn and Fe–35Mn alloy coupons have different phase compositions on the top and bottom faces. The top face exhibited a mixture of ferrite and austenite phases, while the bottom face is composed entirely of austenite. Manganosite (MnO, cubic) is present in both the top and bottom faces. The pure iron sample is composed entirely of a ferrite phase.

The diffractograms of the bottom side of the Fe–30Mn samples are similar to the results obtained from both the top and bottom surfaces of the Fe–29Mn–2Ag and Fe–28Mn–5Ag samples (Fig. 4). All are composed mainly of the austenite phase with some manganosite (MnO) also present as indicated by the low relative intensity reflections. Silver reflections are also shown in the diffractograms for the Fe–29Mn–2Ag and Fe–28Mn–5Ag samples with a low intensity for the main peak reflection at $2\theta = 38.3^{\circ}$.

When considering the bottom side of the non-pressed samples (Fig. 5), both the Fe–30Mn and Fe–35Mn samples as well as the Fe–29Mn–2Ag and Fe–28Mn–5Ag samples present diffractograms showing a pure austenitic phase. A low intensity reflection of silver at $2\theta = 38.3^{\circ}$ is also present in the diffractograms of the Fe–29Mn–2Ag and Fe–28Mn–5Ag samples. A minor reflection on the Fe–30Mn sample, which could not be indexed is present at $2\theta = 35^{\circ}$. The non-pressed Fe sample shows a purely ferritic phase.

3.2. Scanning electron microscopy

Prior to sintering (Fig. 6) the pressed powder particles are seen to be still disjoint with no surface diffusion between one particle and another. This observation changed for the pressed powders post sintering (Figs. 7 and 8), in which condition a large amount of diffusion occurs, such that the surface has no individual particles showing and shows a homogeneous and uniform topography. This is apparent in both the low magnification and high magnification (Figs. 7 and 8) micrographs. The darker areas around the pores, observed in Fe–30Mn and Fe–35Mn coupons (Fig. 7, were determined to be manganese oxides by means of Energy Dispersive X-ray Spectroscopy (EDS).

Only the micrographs representative of the bottom surfaces are presented in this work for simplification. The bottom side was chosen because no micrographs for the top of the unpressed coupons could be obtained due to the lack of a pressing process, causing the top side of the final coupon to be very uneven and rough. The bottom face of each coupon is of greatest interest for this study since it presents a fully austenitic phase composition, which is ideal for osteo applications *in vivo*.

The amount of silver present in the samples can be seen to increase very clearly, where the Fe–29Mn–2Ag sample has fewer white areas compared to the Fe–28Mn–5Ag sample, refer to Fig. 8. The white areas were found to be composed entirely of silver such that all the silver was found to segregate to several areas and present itself as an agglomerate. The difference in colour is due to the difference in the molar mass of the silver compared to the Fe–Mn alloy which therefore shows up due to the

Table 3
Oxide molar masses and alloy molar masses.

Sample	Percentage Oxides Ratio	Oxide Molar mass (g/mol)	Alloy Molar mass (g/mol)
Fe	100% Fe_2O_3	159.7	55.8
Fe–30Mn	70% Fe_2O_3 + 30% MnO	133.1	55.6
Fe–35Mn	65% Fe_2O_3 + 35% MnO	128.6	55.5
Fe–29Mn–2Ag	70% Fe_2O_3 + 30% MnO	133.1	55.6
Fe–28Mn–5Ag	70% Fe_2O_3 + 30% MnO	133.1	55.6

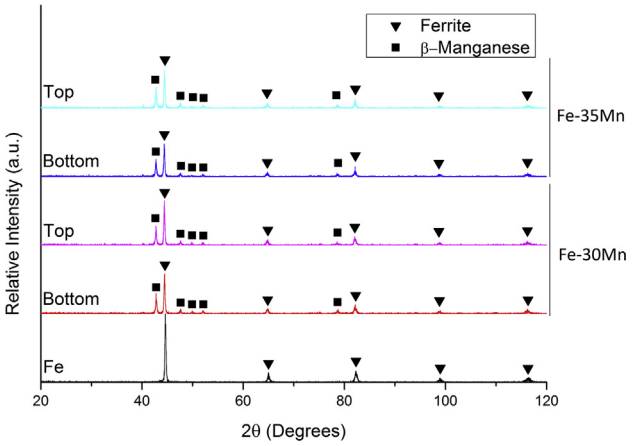

Fig. 2. X-Ray diffractograms of unsintered, pressed Fe, Fe–30Mn and Fe–35Mn coupons.

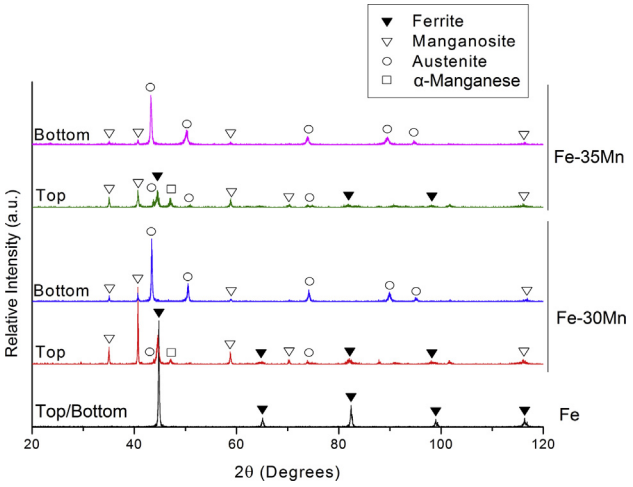

Fig. 3. X-Ray diffractograms of polished, pressed and sintered Fe, Fe–30Mn and Fe–35Mn, for both the top and bottom surfaces.

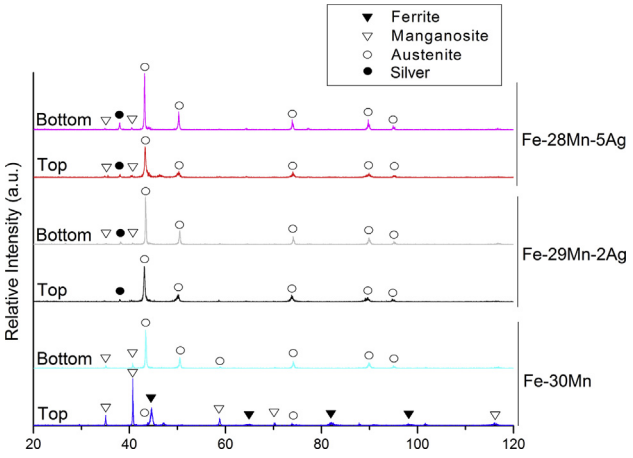

Fig. 4. X-Ray diffactograms of the top and bottom surfaces of polished, pressed and sintered Fe–30Mn, Fe–29Mn–2Ag and Fe–28Mn–5Ag coupons.

intrinsic elemental contrast of the backscatter technique.

Non-pressed samples (Figs. 9 and 10) show a larger number of pores compared to the pressed samples. The samples including silver also show white segregations of silver (Fig. 10) analogous to the pressed samples.

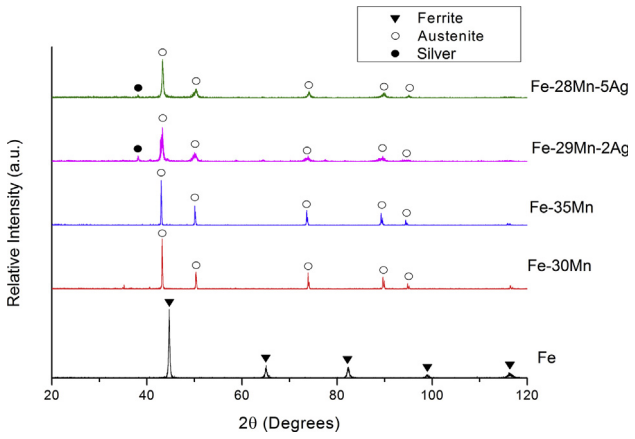

Fig. 5. X-Ray diffractograms of bottom face of polished, non-pressed sintered Fe, Fe–30Mn, Fe–35Mn, Fe–29Mn–2Ag and Fe–28Mn–5Ag coupons.

Fig. 11 presents the percentage area porosity for both the pressed and unpressed samples. The porosiy recorded for the top face of each of the pressed and sintered samples was seen to be greater than that for the bottom of the same sample. The porosity for the pressed and sintered Fe–30Mn and Fe–35Mn is seen to be greater than that for the Fe sample on both the top and bottom faces. Pressed and sintered silver bearing alloys then displayed greater porosity than the non-silver-bearing pressed and sintered alloy counterparts on each of the faces, respectively. The non-pressed samples show porosities which are between 5 to 9 times higher than those of the pressed samples with the same elemental composition.

3.3. *Corrosion testing*

The OCP of each of the samples is shown in Fig. 12. No difference was recorded between the OCP value for the top and bottom face for each of the samples. A significant drop in OCP was measured for the samples containing silver as compared to the samples without silver in their microstructure. No difference can be seen between the non-silver-bearing samples, namely Fe, Fe–30Mn and Fe–35Mn. The OCP of the silver bearing samples, namely Fe–29Mn–2Ag and Fe–28Mn–5Ag, can also be seen to be similar.

From the plots of current against potential for Fe, Fe–30Mn and Fe–35Mn, Fe–29Mn–2Ag and Fe–28Mn–5Ag coupons, the corrosion current was calculated by considering ASTM G102-89 [24] and plotted in Figs. 13 and 14. The corrosion current of Fe on the top and bottom side was seen to be similar to the corrosion current of the Fe–30Mn and Fe–35Mn coupon on the top surface. These corrosion currents were seen to be higher than the corrosion currents recorded on the bottom surfaces of the Fe–30Mn and Fe–35Mn coupons, with the latter two surfaces displaying similar corrosion currents (Fig. 13).

The corrosion current result for the silver bearing samples in Fig. 14 shows similar corrosion currents for the top and bottom faces for each sample with all values being well within each other's error span. The values are seen to be greater than those obtained for the bottom face of the Fe–30Mn coupon.

The results from static immersion degradation tests are shown in Figs. 15 and 16, respectively. The percentage mass loss calculated from Eq. (2), is lower in the pressed samples compared to the non-pressed samples. The greatest difference between the pressed and non-pressed samples is found when comparing the Fe samples where a difference greater than 1600% was recorded when the mass lost due to corrosion was measured in both the BSA solution and in the PBS solution. The difference for the Fe–30Mn and Fe–35Mn alloys was seen to decrease drastically with the coupons showing a difference of 112 ± 21% when exposed to the BSA solution and 44 ± 22% when exposed to the PBS

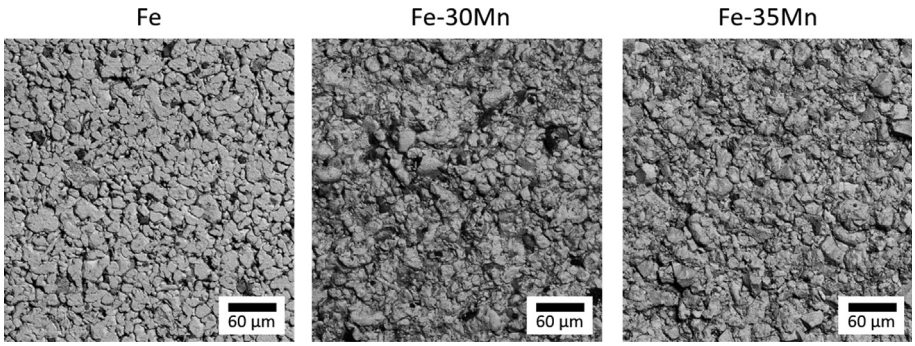

Fig. 6. Backscatter micrographs of non-sintered, pressed Fe, Fe–30Mn and Fe–35Mn coupons.

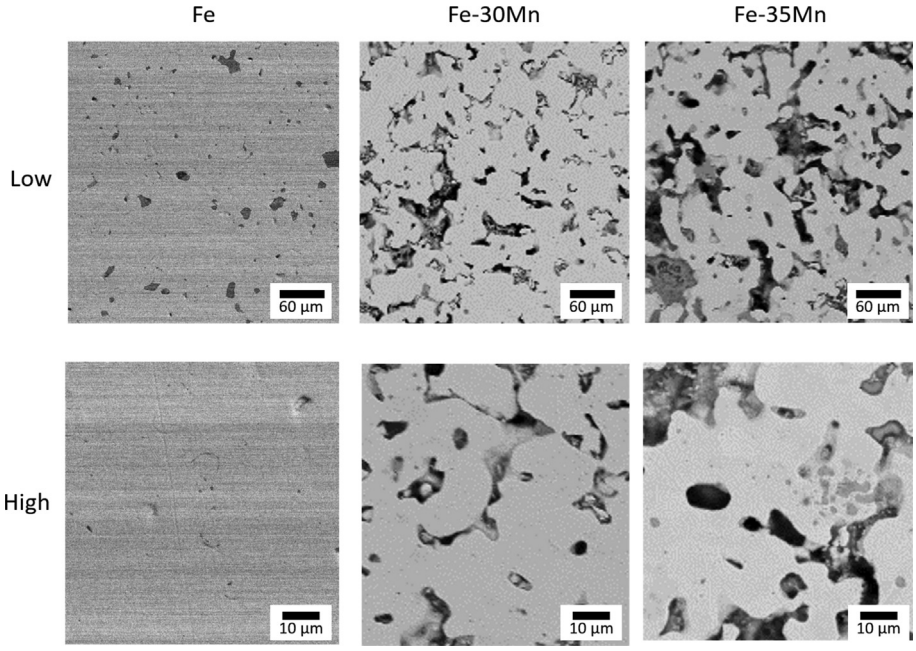

Fig. 7. Backscatter micrographs of sintered, pressed Fe, Fe–30Mn and Fe–35Mn coupons at low and high magnifications.

solution. When adding silver, both the Fe–29Mn–2Ag and Fe–28Mn–5Ag samples showed a difference of 178^{+16}_{-15}% between the pressed and non-pressed samples in both the PBS and the BSA solution. All percentage mass losses in PBS and BSA solutions were similar for each material.

4. Discussion

4.1. The effect of manganese and silver addition on phase composition

Prior to sintering, diffractograms of the green coupons showed that the austenite phase was not present. The latter rather presented the ferritic phase characteristic of the iron powder and an β-manganese phase characteristic of the starting manganese powder (Fig. 2). Thus, the pressing step alone did not give rise to phase transformation in Fe–Mn and Fe–Mn–Ag alloys.

When considering the sintered samples, iron gave a purely ferritic structure. When manganese was added to iron, both at 30 wt.% and at 35 wt.%, an austenite phase formed both on the top and bottom surfaces of the pressed and non-pressed coupons (Fig. 3). This implies that with or without pressing, the diffusion rate during the sintering cycle was high enough to produce an austenitic phase. Manganese was thus observed to act as an austenite stabiliser in Fe–Mn alloys as also reflected in Fe–Mn phase diagrams present in literature [25].

The top surface of the pressed coupons was composed of a mixture of ferrite and austenite while the bottom surfaces of the same coupons were composed solely of an austenite phase (Fig. 3). The difference in phase composition might have been caused as a consequence of formation of larger amounts of manganosite on the top surface of the coupon as shown in the EDS results of the unground surface presented in Table 4. Due to sealing limitations of the equipment used, the reducing gas may have had small partial pressures of oxygen which may have reacted with manganese on the top surface of the sample whilst the bottom surface of the sample was protected due to its position, namely the alumina plate, sample holder interface. Salak et al. [26] show that this reaction occurs due to extremely high furnace temperatures. In fact, even in highly reducing hydrogen atmospheres, the authors find evidence of oxidation of sublimed Mn at temperatures as low as 400 °C. This caused the percentage of free manganese available within the grains closer to the top surface to decrease, causing a bi-phasic structure composed of austenite and ferrite with the latter phase being formed due to Mn starvation.

The phenomenon is also seen on the non-pressed samples (bottom) where once again a purely austenitic structure was observed. This is because the only observable face for the non-pressed sample is the "bottom" face as the top face was irregular due to the lack of a prior pressing process. In addition to this, the sample was protected from the gas convection current on all sides virtue of the TiN coated stainless steel sample holder.

The central part of the pressed coupon contains small pores which are

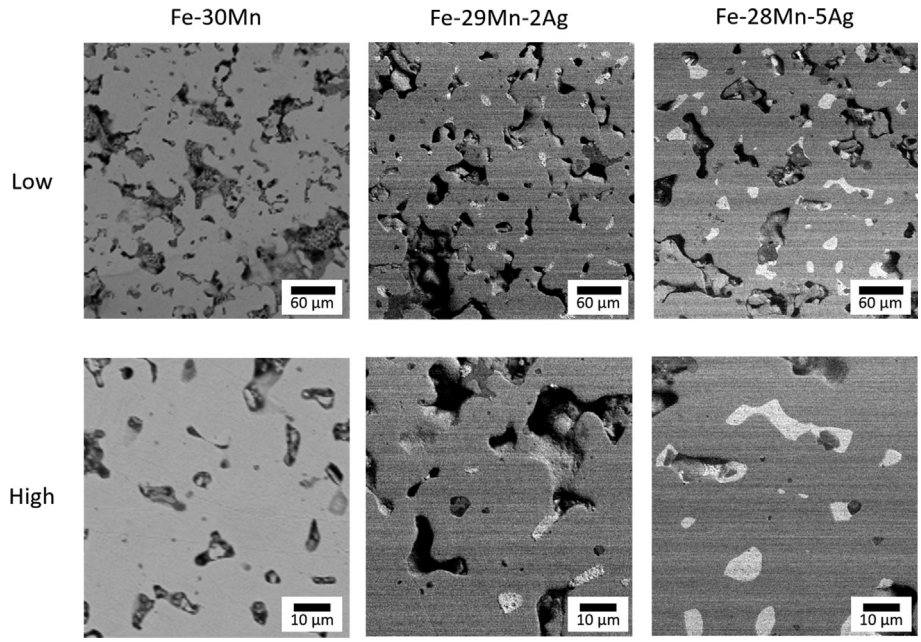

Fig. 8. Backscatter micrographs of sintered, pressed Fe–30Mn, Fe–29Mn–2Ag and Fe–28Mn–5Ag coupons at low and high magnification.

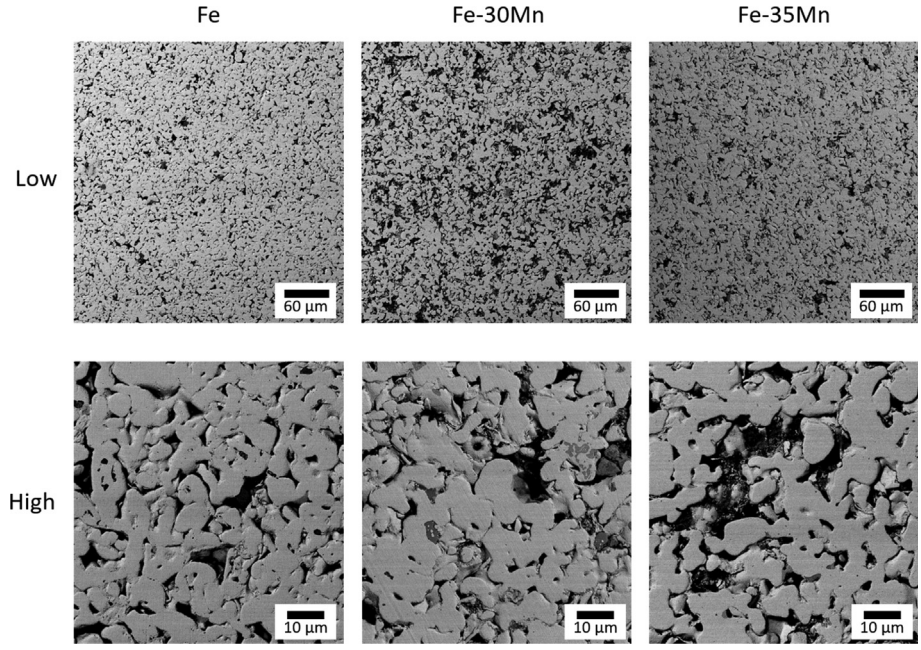

Fig. 9. Backscatter micrographs of sintered, non-pressed Fe, Fe–30Mn and Fe–35Mn coupons at low and high magnification.

not interconnected. A self-inhibitory mechanism may have prevented the formation of a bi-phasic structure in this area. Due to the presence of oxygen within the pores, the Mn on the surface of these pores sublimes and oxidises to MnO as described by Salak et al. [26] and Hryha et al. [27]. The oxidised Mn then re-solidifies and deposits back as a solid within the pore [27]. This reaction causes the depletion of Mn at the surface of the pore and thus causes free Mn to diffuse to the surface of the pore in order to replace the now consumed Mn. However, the lack of interconnectivity of the central pores very little oxygen is available, thus starving the Mn oxidation reaction. This will therefore leave sufficient Mn in the microstucture for the formation of the austenitic phase.

When adding silver, no phase changes were observed, but as reported by others the silver segregated away from the austenitic phases into completely separate pure silver phases. This is because silver is non-miscible with the other metals in the alloy [28]. These phases were observed as white inclusions throughout the microstructure as seen in the backscatter images presented in Figs. 8 and 10. The presence of a pure silver phase can also be observed in the X-ray diffractograms (Figs. 4 and 5) which show peaks of the silver phase in its pure form. The evidence was strengthened by EDS analysis which showed the presence of pure silver phases throughout the coupons. Since the melting temperature of silver is 961.93 °C, at standard pressure [29], and sintering was carried out at 1200 °C, the silver was liquified during sintering and took up the shape of the space available, filling pores in the alloy coupon. Theoretically, the pores were filled out staring from, the smallest pore, then progressing to larger pores of the green [30]. This phenomenon may

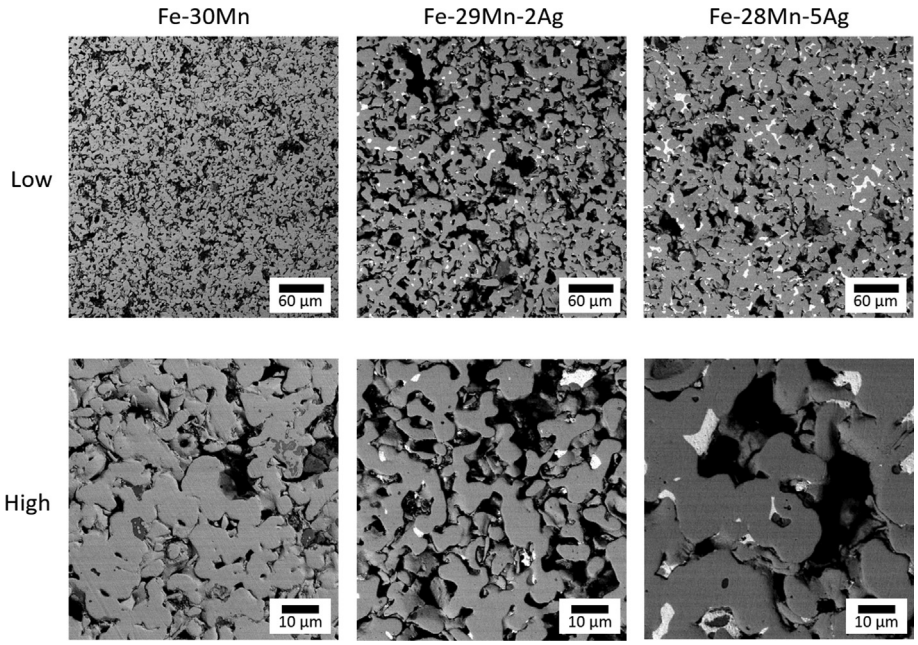

Fig. 10. Backscatter micrographs of sintered, non-pressed Fe–30Mn, Fe–29Mn–2Ag and Fe–28Mn–5Ag coupons at low and high magnification.

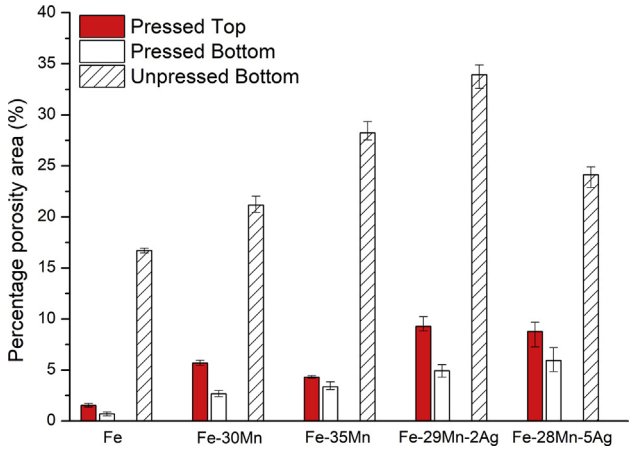

Fig. 11. Percentage porosity area for the pressed and non-pressed samples ($n = 3$). Error bars represent the maximum and minimum porosity values.

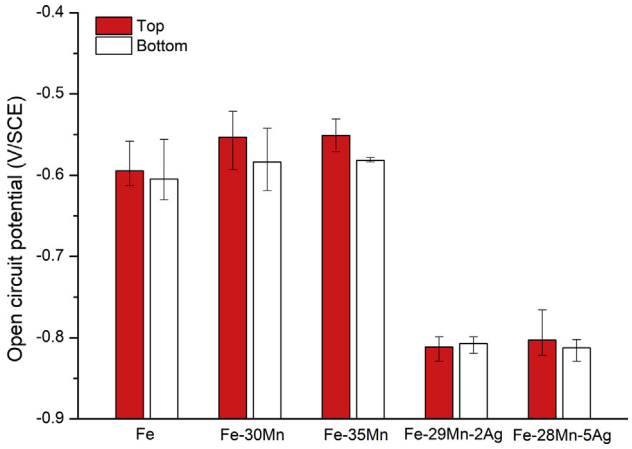

Fig. 12. OCP value of pressed and sintered Fe, Fe–30Mn, Fe–35Mn, Fe–29Mn–2Ag and Fe–28Mn–5Ag measured over 1 h. Error bars are representative of the maximum and minimum value obtained for $n = 3$ samples.

explain the difference between the microstructure observed for Fe–29Mn–2Ag and Fe–28Mn–5Ag samples in Figs. 8 and 10. This is as expected since in liquid-phase sintering, the liquid phase is expected to fill smaller pores first due to the higher capillary action for the wetting liquid [30]. The overall porosity of Ag bearing samples increases by small amounts compared to the non-silver-bearing samples as shown in Fig. 11. This is because post melting, the volume occupied by the silver decreases as any spaces between the particles are eliminated thus giving rise to the marginally higher porosity observed in Fig. 11.

The pores left behind on the Fe–29Mn–2Ag and Fe–28Mn–5Ag samples of the pressed coupons, are larger than those present on the Fe–30Mn sample. The reason for this may be that silver particles had agglomerated into larger particles prior to sintering. Upon melting, the silver is driven by capillarity to fill smaller pores, leaving the space previously occupied by the agglomerated silver particles devoid of silver [30].

The silver bearing coupons showed an austenite phase both on the top and bottom surfaces (Fig. 4). This could have been due to the action of molten silver during liquid phase sintering which coat the sample, thus protecting manganese from oxidation at the surface.

4.2. The effect of phase composition on corrosion rate

From potentiodynamic corrosion test results it was found that when comparing corrosion currents on the Fe–Mn alloys, the top surfaces of the Fe–30Mn and Fe–35Mn coupons had a higher corrosion current than the bottom surfaces (Fig. 13). This can be attributed to the fact that top surfaces show two phases which act as micro galvanic couples. The bottom face on the other hand is composed solely of an austenitic phase. This phenomenon is further proved by the results in Fig. 14. Here the corrosion current of the top and bottom surfaces of the silver bearing coupons, namely Fe–28Mn–5Ag and Fe–29Mn–2Ag were found to be similar, owing to the purely austenitic composition that both surfaces have (Fig. 4).

The corrosion current of the bottom surface of Fe–30Mn and Fe–35Mn from potentiodynamic test were lower than those of the Fe coupon. Corrosion current is used as the benchmark rather than corrosion current density since the exposed area of the coupon could not be accurately determined due to the porosity present. This result is not replicated in the static immersion tests with pressed samples in similar

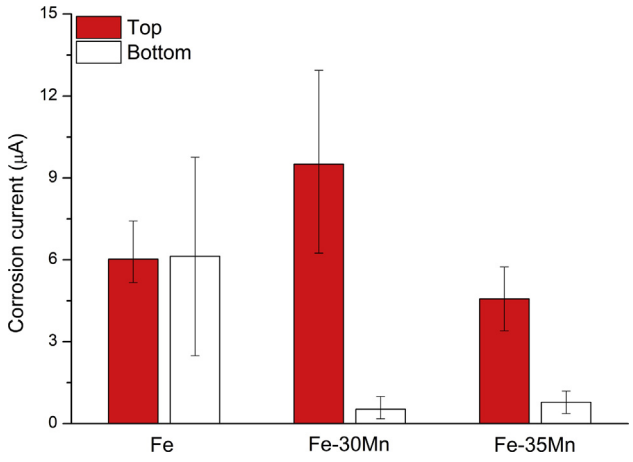

Fig. 13. Calculated corrosion current for pressed and sintered Fe, Fe–30Mn and Fe–35Mn coupons from potentiodynamic testing in BSA solution at 37 °C from $n = 3$ samples. Error bars are representative of maximum and minimum values of each set.

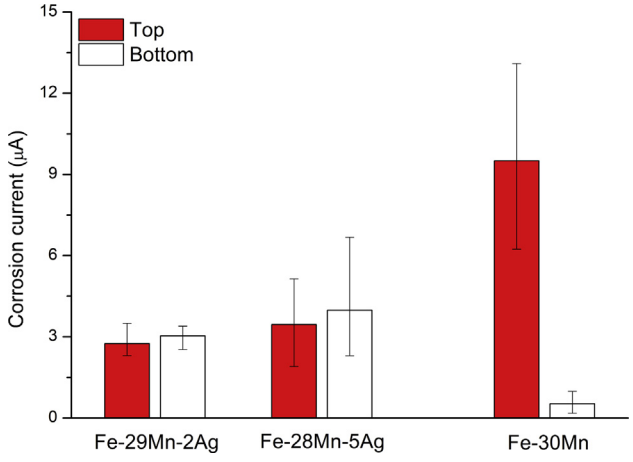

Fig. 14. Calculated corrosion current for pressed and sintered Fe–29Mn–2Ag, Fe–28Mn–5Ag and Fe–30Mn coupons from potentiodynamic testing in BSA solution at 37 °C from $n = 3$ samples. Error bars are representative of maximum and minimum values of each set.

PBS + BSA solution. A number of reasons may explain these results; (1) Sample exposure area: in immersion testing, the whole sample was dipped and thus the overall corrosion rate was affected by the microstructures of the top, bottom and side surfaces. The relative percentage of ferrite and austenite present in the Fe–30Mn and Fe–35Mn coupons have then provided the corrosion rate shown in Fig. 15. (2) Time and method of exposure: the fact that in immersion testing, the sample is dipped in a solution for a number of days implies that the internal porosity is completely filled by the test solution. Given the porosity present in the samples (Fig. 11), certain differences may further be highlighted by the time factor. Since the porosity is not totally interconnected, the sample exposed to the immersion test may have had enough time to corrode metallic walls, thus allowing the solution into pores which were not previously open.

The inclusion of silver into the alloy microstructure in both the Fe–29Mn–2Ag and Fe–28Mn–5Ag samples also acted as a galvanic couple. This was clear when comparing the corrosion current of the Fe–29Mn–2Ag and Fe–28Mn–5Ag samples with that of the Fe–30Mn sample (Fig. 14). The average corrosion current of the silver bearing samples was found to be 648^{+141}_{-116} % that recorded for the bottom surface of the Fe–30Mn coupons. The Fe–29Mn–2Ag, Fe–28Mn–5Ag and

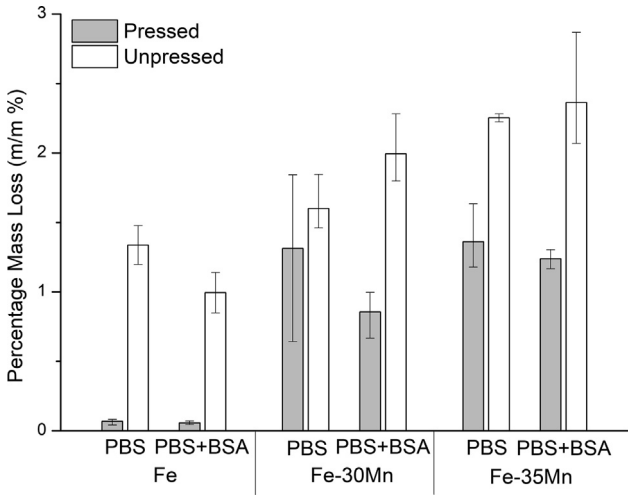

Fig. 15. Percentage mass lost due to corrosion from Fe, Fe–30Mn and Fe–35Mn coupons when exposed to PBS and BSA solutions for 14 days in a 6% CO_2 incubator at 37 °C. $n = 3$ samples. Bars are representative of the average mass lost. Error bars show the maximum and minimum value for each condition.

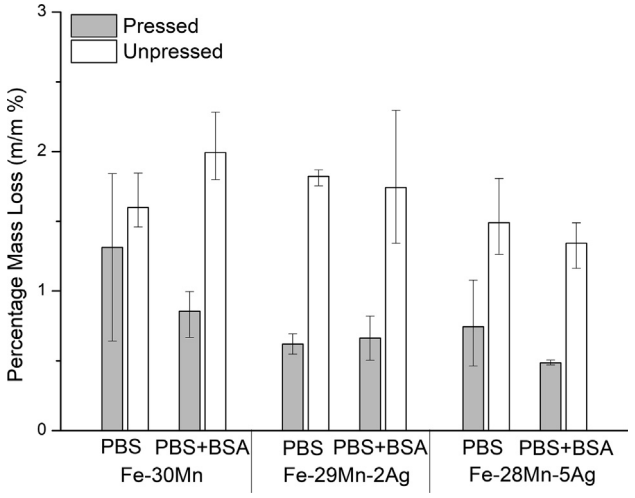

Fig. 16. Percentage mass lost due to corrosion from Fe–30Mn, Fe–29Mn–2Ag and Fe–28Mn–5Ag coupons when exposed to PBS and BSA solutions for 14 days in a 6% CO_2 incubator at 37 °C. $n = 3$ samples. Bars are representative of the average mass lost. Error bars show the maximum and minimum value for each condition.

Table 4
EDS results for top and bottom surfaces of Fe–30Mn alloy post sintering without grinding or polishing. Each value has an error of ±1 wt.%.

Element	Top (wt.%)	Bottom (wt.%)
Fe	47.51	71.20
Mn	41.50	28.80
O	10.99	0.00

Fe–30Mn (bottom) coupon have the same Fe–Mn phase structure (austenitic), allowing for direct comparison between non-silver bearing alloy and the silver bearing alloy. In this regard, comparing the corrosion current of the Fe–29Mn–2Ag and Fe–28Mn–5Ag coupons to the corrosion current of the top surface of the Fe–30Mn alloy would render the comparison void, due to the galvanic effect of the ferrite phase included on this surface.

The results from the static immersion test in Fig. 16 do not reflect the

data from the potentiodynamic test of the bottom side or top side of the silver bearing coupons, respectively. Whereas the results from the static immersion test show a quasi-equal weight loss for the Fe–30Mn, Fe–29Mn–2Ag and Fe–28Mn–5Ag coupons. This phenomenon is once again probably due to the exposure characteristics of the potentiodynamic and static immersion degradation tests. It may be due to the protective effect of this layer on the underlying coupon [3]. The corrosion mechanism for the static immersion test was general corrosion as the surface was covered by an insoluble red-brown hydroxide and hydrated oxide layer $Fe_2O_3.nH_2O$ [31]. This layer was also observed by other authors in the field [3, 31, 32]. The overall degradation mechanism can the be described in a 4 step process as described by Hermawan et al. [31]. The first step initiates the dissolution of Fe and Mn ions into solution. This is then followed by the deposition of an insoluble hydroxide and/or hydrated oxide layer. The imperfections in this formed layer then give rise to a situation where pitting might occur on the sample surface. The final step is then the formation of Ca/P layer, in a coral like structure [31].

4.3. The effect of pressing on corrosion rate

Pressed samples were shown to have a lower corrosion rate compared to non-pressed samples when exposed to static immersion testing both in PBS and BSA solutions (Figs. 15 and 16). This phenomenon was observed on all samples, including Fe, Fe–30Mn, Fe–35Mn, Fe–29Mn–2Ag and Fe–28Mn–5Ag coupons with the exception of Fe–30Mn coupons exposed to the PBS solution, in which the corrosion rate of the pressed and non-pressed samples was seen to be very similar. The higher corrosion rate recorded for the non-pressed samples is due to the larger number and volume of pores observed on the non-pressed coupons (Figs. 9 and 10) compared to those observed on pressed coupons (Figs. 7 and 8). This result is also represented in Fig. 11. The larger area of porosity increases the surface area exposed to the electrolyte solution, thereby increasing the corrosion current. This novel result implies that the corrosion rate of the non-pressed samples is more suited to the application of the alloy structure *in vivo*, since it reduces the time of degradation *in vivo*, thus moving closer to the bone healing time of 6–12 weeks [33]. From a degradation perspective, this proves that the non-pressed alloy is better than the pressed alloy for applications *in vivo*.

4.4. Optimising scaffolds for use in vivo

When considering the face which was not exposed to oxidation of manganese, Fe–30Mn samples displayed an austenitic phase composition both in the pressed (Fig. 3) and non-pressed (Fig. 5) state. This implies that even at 30 wt.% Mn, the alloy was able to achieve a non-magnetic structure, which would be ideal for *in vivo* applications enabling the patient to undergo post-op imaging with magnetic resonance imaging devices. When focusing on the bottom side of the pressed coupons, increasing the Mn concentration to percentages above 30 wt.% was shown to have negligible effect on the corrosion rate both when tested in a potentiodynamic setup (Fig. 13) and also when tested in a static immersion setup (Fig. 15). Similar results were also recorded for the non-pressed coupons when tested in a static immersion setup. This implies that manganese percentages can be kept to 30 wt.% eliminating the need for higher Mn concentrations in the alloy. This would therefore reduce the cost of the scaffold and also decrease the risk of Mn neurotoxicity should scaffold rejection complications be suffered by the patient [34].

Increasing silver inclusions in scaffolds, leads to severe toxicity within the *in vivo* scenario, thus it is desirable that the percentage of silver is kept to a minimum (<2 mg/L) [17]. In the present study it was found that there is no difference in corrosion rate between the Fe–29Mn–2Ag and Fe–28Mn–5Ag samples. This implies that within the sample set presented in this work, the use of lower silver percentages corresponding to 2 wt.% is sufficient and beneficial for *in vivo* applications.

An emerging application of powder metallurgy is the generation of porous scaffolds using reticulated sponges. This technology employs the use of powders adhered to these sponges. The coated sponges are then dried and sintered in a furnace, where the sponge is burnt off [7, 8, 9]. For this application and other similar scaffold generation techniques, non-pressed powders are utilised. In this condition the Fe–Mn–Ag alloys were seen to degrade far more quickly than in the pressed condition (Figs. 15 and 16). This implies a faster degradation rate of the scaffold *in vivo*, which is closer to the desirable bone healing time of 6–12 weeks [33]. This feature would be of great benefit even to the prosthetics industry. Thus the optimal alloy chosen for *in vivo* bone regeneration scaffolds was non-pressed and sintered Fe–30Mn–2Ag.

5. Conclusions

The first hypothesis stating that the addition of a percentage ≥30% Mn to Fe utilised in a non-pressed non-pre-alloyed sintered powder metallurgy part allows the production of a fully austenitic microstructure has been proven and upheld, as a single austenite phase has been generated in the non-pressed samples following sintering.

The second hypothesis which states that the addition of silver to the same non-pressed non-pre-alloyed Fe–Mn alloy would increase the alloy's corrosion rate, has not been upheld since when comparing the percentage mass lost in a SIDT from the non-pressed non-silver-bearing alloy to the non-pressed silver bearing alloy, no difference has been recorded. However, when considering the pressed counterparts and comparing the fully austenitised side of the Fe–30Mn samples to the analogous silver containing samples, an increase in corrosion current of 548^{+141}_{-116} % on average was recorded in a potentiodynamic testing setup. The increase in corrosion current recorded during potentiodynamic testing could help bring the corrosion rate of the Fe–Mn–Ag alloy closer to the rate of osteogenic repair in-vivo.

Since a singular austenite phase was successfully formed in the non-pressed sample, a non-magnetic degradable non-pressed 3D scaffold could be formed using the presented technology. The formation of a fully austenitic structure formed from the sintering of a mixture of elemental metals lends itself well to degradable scaffolding technologies.

The groundwork set out by this work may therefore make it possible to cut the shape of the scaffold required from an easily formable polymeric scaffold, coat the scaffold with a mixture of elemental powder metals and sinter the metallic deposits into an austenitic structure. The addition of silver to the scaffold would then aid in increasing the corrosion rate whilst also providing antibacterial properties.

Declarations

Author contribution statement

Malcolm Caligari Conti: Conceived and designed the experiments; Performed the experiments; Analyzed and interpreted the data; Contributed reagents, materials, analysis tools or data; Wrote the paper.

Emmanuel Sinagra & Pierre Schembri-Wismayer: Analyzed and interpreted the data; Contributed reagents, materials, analysis tools or data.

Bertram Mallia, Joseph Buhagiar & Daniel Vella: Conceived and designed the experiments; Analyzed and interpreted the data; Contributed reagents, materials, analysis tools or data.

Funding statement

Malcolm Caligari Conti was funded by the REACH HIGH Scholars Programme. The research work disclosed in this publication is partially funded by the REACH HIGH Scholars Programme–Post-Doctoral Grants. The grant is part-financed by the European Union, Operational Programme II–Cohesion Policy 2014–2020 Investing in human capital to create more opportunities and promote the wellbeing of

society–European Social Fund.

Competing interest statement

The authors declare no conflict of interest.

Additional information

No additional information is available for this paper.

Acknowledgements

Malcolm Caligari Conti would also like to thank Ms Daphne Anne Pollacco who contributed to experimental procedures by helping in the mixing and preparation of elemental powders and coupons, image analysis, providing a scientific background for the selection of electrolytes for SIDT and PD testing and review of the final article.

References

[1] T. Ghassemi, A. Shahroodi, M.H. Ebrahimzadeh, A. Mousavian, J. Movaffagh, A. Moradi, Current concepts in scaffolding for bone tissue engineering, Archiv. Bone Jt. Surg. 6 (2018) 90.
[2] F. Zivic, N. Grujovic, E. Pellicer, J. Sort, S. Mitrovic, D. Adamovic, et al., Biodegradable metals as biomaterials for clinical Practice: iron-based materials, in: Biomaterials in Clinical Practice, Springer, 2018, pp. 225–280.
[3] H. Hermawan, D. Dube, D. Mantovani, Degradable metallic biomaterials: design and development of Fe-Mn alloys for stents, J. Biomed. Mater. Res. A 93 (Apr 2010) 1–11.
[4] Y.P. Feng, N. Gaztelumendi, J. Fornell, H.Y. Zhang, P. Solsona, M.D. Baró, et al., Mechanical properties, corrosion performance and cell viability studies on newly developed porous Fe-Mn-Si-Pd alloys, J. Alloy. Comp. 724 (2017) 1046–1056.
[5] H. Hermawan, D. Dubé, D. Mantovani, Development of degradable Fe-35Mn alloy for biomedical application, Adv. Mater. Res. 15–17 (2006) 107–112.
[6] R. Alavi, A. Trenggono, S. Champagne, H. Hermawan, Investigation on mechanical behavior of biodegradable iron foams under different compression test conditions, Metals 7 (2017) 202.
[7] R. Oriňáková, A. Oriňák, L.M. Bučková, M. Giretová, Ľ. Medvecký, E. Labbanczová, et al., Iron based degradable foam structures for potential orthopedic applications, Int. J. Electrochem. Sci 8 (2013) 12451–12465.
[8] P. Quadbeck, K. Kümmel, R. Hauser, G. Standke, J. Adler, G. Stephani, et al., Structural and material design of open-cell powder metallurgical foams, Adv. Eng. Mater. 13 (2011) 1024–1030.
[9] G. Stephani, O. Andersen, H. Göhler, C. Kostmann, K. Kümmel, P. Quadbeck, et al., Iron based cellular structures – status and prospects, Adv. Eng. Mater. 8 (2006) 847–852.
[10] B. Liu, Y.F. Zheng, Effects of alloying elements (Mn, Co, Al, W, Sn, B, C and S) on biodegradability and in vitro biocompatibility of pure iron, Acta Biomater. 7 (Mar 2011) 1407–1420.
[11] M. Schinhammer, A.C. Hänzi, J.F. Löffler, P.J. Uggowitzer, Design strategy for biodegradable Fe-based alloys for medical applications, Acta Biomater. 6 (2010) 1705–1713.
[12] R.-Y. Liu, R.-G. He, L.-Q. Xu, S.-F. Guo, Design of Fe–Mn–Ag alloys as potential candidates for biodegradable metals, Acta Metall. Sin. 31 (2018) 584–590.
[13] H. Hermawan, H. Alamdari, D. Mantovani, D. Dubé, Iron–manganese: new class of metallic degradable biomaterials prepared by powder metallurgy, Powder Metall. 51 (2013) 38–45.
[14] B. Wegener, B. Sievers, S. Utzschneider, P. Müller, V. Jansson, S. Rößler, et al., Microstructure, cytotoxicity and corrosion of powder-metallurgical iron alloys for biodegradable bone replacement materials, Mater. Sci. Eng., B 176 (2011) 1789–1796.
[15] P. Quadbeck, R. Hauser, K. Kümmel, G. Standke, G. Stephani, B. Nies, et al., Iron based cellular metals for degradable synthetic bone replacement, in: PM2010 World Congress, Florenz, Italy, 2010.
[16] P. Sotoudehbagha, S. Sheibani, M. Khakbiz, S. Ebrahimi-Barough, H. Hermawan, Novel antibacterial biodegradable Fe-Mn-Ag alloys produced by mechanical alloying, Mater. Sci. Eng. C 88 (2018) 88–94.
[17] S. Chernousova, M. Epple, Silver as antibacterial agent: ion, nanoparticle, and metal, Angew. Chem. Int. Ed. 52 (2013) 1636–1653.
[18] M. Goly, S. Skrzypek, Surface layer characterisation of bearing rings, Archiv. Mater. Sci. 662 (2007) 662.
[19] R. Forbes, A. Cooper, H. Mitchell, The composition of the adult human body as determined by chemical analysis, J. Biol. Chem. 203 (1953) 359–366.
[20] X. Feng, Chemical and biochemical basis of cell-bone matrix interaction in health and disease, Curr. Chem. Biol. 3 (2009) 189–196.
[21] F. Petchey. Bone. Available: http://www.c14dating.com/bone.html. Accessed: 17/2/2019.
[22] G. Astm, Standard test method for conducting potentiodynamic polarization resistance measurements, Annu. Book ASTM (Am. Soc. Test. Mater.) Stand. 3 (2009) 237–239.
[23] M.C. Conti, D. Aquilina, C. Paternoster, D. Vella, E. Sinagra, D. Mantovani, et al., Influence of cold rolling on in vitro cytotoxicity and electrochemical behaviour of an Fe-Mn-C biodegradable alloy in physiological solutions, Heliyon 4 (2018), e00926.
[24] G. ASTM, Standard Practice for Calculation of Corrosion Rates and Related Information from Electrochemical Measurements, G102-89, ASTM International, West Conshohocken, USA, 2004.
[25] P. Wang, J. Zhao, Y. Du, H. Xu, T. Gang, J. Fen, et al., Experimental investigation and thermodynamic calculation of the Fe–Mg–Mn and Fe–Mg–Ni systems, Int. J. Mater. Res. 102 (2011) 6–16.
[26] A. Šalak, M. Selecká, Manganese in Powder Metallurgy Steels, Springer Science & Business Media, 2012.
[27] E. Hryha, E. Dudrova, The sintering behaviour of Fe-Mn-C powder system, correlation between thermodynamics and sintering process, Mn distribution and microstructure, in: Materials Science Forum, 2007, pp. 761–764.
[28] Calculated Ag-Fe phase diagram. Available: http://resource.npl.co.uk/mtdata/phdiagrams/agfe.htm. Accessed: 17/2/2019.
[29] J.F. Shackelford, Y.-H. Han, S. Kim, S.-H. Kwon, CRC Materials Science and Engineering Handbook, CRC press, 2016.
[30] R.M. German, Liquid Phase Sintering, Springer Science & Business Media, 2013.
[31] H. Hermawan, A. Purnama, D. Dube, J. Couet, D. Mantovani, Fe-Mn alloys for metallic biodegradable stents: degradation and cell viability studies, Acta Biomater. 6 (May 2010) 1852–1860.
[32] H. Hermawan, Metallic biodegradable coronary stent: degradation study, in: Biodegradable Metals, Springer, 2012, pp. 49–57.
[33] K.W. Krannitz, H.W. Fong, L.M. Fallat, J. Kish, The effect of cigarette smoking on radiographic bone healing after elective foot surgery, J. Foot Ankle Surg. 48 (2009) 525–527.
[34] T.R. Guilarte, Manganese neurotoxicity: new perspectives from behavioral, neuroimaging, and neuropathological studies in humans and non-human primates, Front. Aging Neurosci. 5 (2013) 23.